Site occupancy and electric-field induced strain response of Er-doped (Bi0.4Na0.4Sr0.2)TiO3 ceramics

MCLAUGHLIN, Kerry, PASCUAL-GONZALEZ, Cristina, WANG, Dawei and FETEIRA, Antonio <http://orcid.org/0000-0001-8151-7009>

Published version

MCLAUGHLIN, Kerry, PASCUAL-GONZALEZ, Cristina, WANG, Dawei and FETEIRA, Antonio (2019). Site occupancy and electric-field induced strain response of Er-doped (Bi0.4Na0.4Sr0.2)TiO3 ceramics. Journal of Alloys and Compounds, 779, 7-14.

Site occupancy and electric-field induced strain response of Er-doped $(Bi_{0.4}Na_{0.4}Sr_{0.2})TiO_3$ ceramics

Kerry McLaughlin[1,2], Cristina Pascual-Gonzalez[1], Dawei Wang[2] and Antonio Feteira[1]

[1]Christian Doppler Lab on Advanced Ferroic Oxides, Materials Engineering and Research Institute, Sheffield Hallam University, Howard Street, S1 1WB, Sheffield, UK.

[2]Department of Materials Science and Engineering, The University of Sheffield, Mappin Street, S1 4JD, Sheffield, UK

Abstract

Er-doped $(Bi_{0.4}Na_{0.4}Sr_{0.2})TiO_3$ powders were prepared by solid state reactions according to A-site donor $(Bi_{0.4-x/3}Na_{0.4-x/3}Sr_{0.2-x/3}Er_x)TiO_3$ (x=0. 0.015 and 0.02) and B-site acceptor $(Bi_{0.4}Na_{0.4}Sr_{0.2})Ti_{1-y}Er_yO_3$ (y=0, 0.015 and 0.02) substitutional doping mechanisms. In both cases, room-temperature X-ray diffraction analyses revealed a decrease of the unit cell volume with increasing Er contents, suggesting A-site occupancy to be thermodynamically more favourable. Over the 25-175 °C temperature range, A-site doped ceramics, in particular x=0.015, showed enhanced thermal stability of the maximum achievable electric-field induced strain. Importantly, this minor doping level also reduced dielectric losses at high temperature and lead to a transition from non-ergodic to ergodic relaxor behaviour. These results may further motivate the study of the impact of other minor dopants in this family of Pb-free piezoceramics.

1-Introduction

Piezoceramics convert electric fields into mechanical strains, but also mechanical stresses into electric polarization. This reciprocal behaviour enables their deployment in a vast range of sensing and actuating technologies. Currently, piezoelectric technologies rely mainly on ferroelectric $PbZr_xTi_{1-x}O_3$-based (PZT) ceramics, particularly on compositions near the so-called morphotropic phase boundary (MPB) at x =0.52. Nevertheless, European Union directives limiting the use of toxic heavy metals (such as Pb) in electronics have been driving the search for alternatives to PZT piezoceramics.[1] Many investigators focused their search in $Bi_{0.5}Na_{0.5}TiO_3$–based piezoceramics[2-9], but other compounds such as $Bi_{0.5}K_{0.5}TiO_3$ [10], $K_{0.5}Na_{0.5}NbO_3$ [11-13], $KNbO_3$[14-16] and $BiFeO_3$.

$Bi_{0.5}Na_{0.5}TiO_3$ (BNT) is a well-known relaxor ferroelectric with a remnant polarisation of P_r =38 $\mu C/cm^2$. Unfortunately, BNT also shows a large coercive field of ~70 kV/cm, which makes poling a problematic process. In order to circumvent this drawback and optimize the electromechanical properties of BNT, researchers have been exploring solid solutions of BNT with other Pb-free ferroelectrics. Among those, $Bi_{0.5}Na_{0.5}TiO_3$–$BaTiO_3$ (BNT-BT) and $Bi_{0.5}Na_{0.5}TiO_3$–$SrTiO_3$ (BNT-ST) solid solutions have received considerable attention.[17-19]

The (1−*x*)BNT–*x*ST system is particularly interesting, because ST appears to effectively reduce the coercive field of BNT. Moreover, Hiruma et al[20] showed that for *x* = 0.26 the maximum field-induced strain can reach 0.30 % at 60 kV/cm. Later, Krauss et al[21] carried out a comprehensive characterisation of the electromechanical behaviour of (1−*x*)BNT–*x*ST ceramics and they confirmed a maximum electric-field induced strain of 0.39% (at 60 kV/cm) to occur at x=0.25. In addition, they also showed the strain for x=0.20 to increase from 0.22% at room temperature reaching a maximum of 0.25% at 100°C, and then to

decrease dramatically to 0.15% at 150°C. More recently, Acosta et al[22] carried a very detailed study on the temperature- and frequency-dependency of the properties of x=0.25 ceramics and also observed the unipolar strain to decrease with increasing temperatures, however more dramatically when compared with data for x=0.20. The crystal structure of BNT-STx ceramics was re-analysed by Kim et al[23] using X-ray diffraction and neutron scattering data. Their Rietveld structural refinements suggest the crystal structure to successively change with increasing x from rhombohedral (x = 0.00) to rhombohedral and tetragonal (x = 0.10–0.30), tetragonal and cubic (x = 0.40–0.60), and finally cubic (x = 0.80–1.00). Koruza et al[24] also investigated effect of processing temperatures and times on the formation and disappearance grains featuring a core-shell microstructure in ceramics with x=0.25. The impact Fe-and Nb-doping on (1–*x*)BNT–*x*ST ceramics within the x=0.23 to 0.25 compositional range was recently investigated. Cho et al[25] studied the crystal structure, domain patterns and electromechanical behaviour of Fe-modified BNT-ST [$0.77(Bi_{0.5}Na_{0.5})TiO_3$-$0.23Sr(Ti_{1-x}Fe_x)O_3$] ceramics. In the undoped ceramics, they observed the formation of a core-shell microstructure, where the crystal structures of the core and shell regions are rhombohedral and tetragonal, respectively. Nevertheless, the relative volume of the core region appears to decrease with the substitution of Ti^{4+} by Fe^{3+}, which is also accompanied by a transformation from a ferroelectric to ergodic relaxor behaviour. This B-site doping mechanism improved the effective piezoelectric coefficient, d_{33}*, from 290 pm/V for the base BNT-23ST composition to over 500 pm/V at 2 kV/mm for the x=0.02 composition.

Also recently, Zaid and Feteira[26] showed Er-minor doping to be an effective method to enhance the temperature stability of the electroresponse of BNT-BKT-BT ceramics. The present work evaluates the impact of minor Er substitutions in ceramics prepared according

to A-site donor $(Bi_{0.4-x/3}Na_{0.4-x/3}Sr_{0.2-x/3}Er_x)TiO_3$ (x=0. 0.015 and 0.02) and B-site acceptor $Bi_{0.4}Na_{0.4}Sr_{0.2}(Ti_{1-y}Er_y)O_3$ (y=0. 0.015 and 0.02) substitution mechanisms. The choice of $(Bi_{0.4}Na_{0.4}Sr_{0.2})TiO_3$ as the parent composition was motivated from a previous work by Krauss et al[21], who studied in detail the BNT-ST system. In their work, this composition is shown to exhibit a combination of electrostrictive and ferroelectric components, the latter typified by a negative bipolar strain, which is associated with domain switching. Here, it is anticipated that chemical substitution, is likely to increase the chemical disorder in this composition and consequently to enhance the electrostrictive response. X-ray diffraction data reveals that under the chosen processing conditions, A-site incorporation of Er is favoured in relation to B-site. Subsequently, studies of the electrical field response of A-site doped ceramics in the 25-175 °C temperature range showed an enhancement of both the maximum achievable electric-field induced strain and its temperature stability, in particular for 1.5 mol% Er-doped ceramics. Doping is also responsible for a transition from a non-ergodic to an ergodic relaxor response. Finally, Er doping also favourably reduces the high temperature dielectric losses.

2-Experimental procedure

$(Bi_{0.4}Na_{0.4}Sr_{0.2})TiO_3$ (BNT-20ST) and Er-doped ceramics were prepared by the solid state reaction route according the A-site donor $(Bi_{0.4-x/3}Na_{0.4-x/3}Sr_{0.2-x/3}Er_x)TiO_3$ (x=0, 0.015 and 0.02) and B-site acceptor $Bi_{0.4}Na_{0.4}Sr_{0.2}(Ti_{1-y}Er_y)O_3$ (y=0, 0.015 and 0.02) formulas. Starting reagents Bi_2O_3, Na_2CO_3, $SrCO_3$, TiO_2 and Er_2O_3 (Sigma Aldrich, UK, ACS reagent, >99%) were mixed in polypropylene (PP) bottles with yttria-stabilised zirconia milling media and propan-2-ol as solvent and milled overnight. The obtained slurries were dried, sieved through a 250

mesh stainless steel sieve and calcined at 850 ºC for 2 hours using a cooling/heating rate of 5°C/min. Purity and crystal structures were studied using an X-ray diffractometer (model: Empyrean, Panalytical™, Almelo, The Netherlands, $K_{\alpha 1}$-Cu line at λ = 1.54060 Å) operated at a voltage of 40 kV and a current of 40 mA, and using a step size 0.01º 2θ in the 20 to 80 2θ range. Lattice parameters were refined using a least squares method. Depolarized Raman spectra were obtained in back-scattering geometry using a micro-Raman spectrometer (model: DXR™ 2, Thermo Fisher Scientific, Paisley, UK), equipped with a Rayleigh line-rejection edge filter that was set for the 532 nm excitation of an Ar^+ ion laser, which allowed ripple-free measurements down to 50 cm^{-1} from the laser line. Spectra were acquired using a 10× microscope objective and a laser power of 0.1 to 1 mW.

Pellets were uniaxially-pressed under an applied pressure of ~ 200 MPa and sintered at 1250 ºC for 2 hours, using a heating/cooling rate of 5°C/min. The microstructures were examined using a scanning electron microscope (model: Nova, FEI, The Netherlands, field emission gun) operated at 20 kV. Samples were gold sputtered to avoid charging under the electron beam.

The sintered ceramics were ground using 2500 grade SiC paper. Silver electrodes were applied onto both surface. The temperature-dependence of the relative permittivity and dielectric loss was measured for poled and unpoled ceramics. Poling was conducted under an applied electric field of 40 kV/cm for 20 minutes. Small signal piezoelectric properties were measured by the Berlincourt method.

Electric field-induced polarisation and strain were measured using a commercial ferroelectric/piezoelectric measuring system (model TF analyser 200, AixACCT Systems GmbH, Aachen, Germany). For all polarisation and strain measurements, triangular waves at

1 Hz frequency were employed as the high voltage input. Sample's current response was measured by applying an electrical voltage excitation signal using the precise virtual ground method. Electric-field induced displacement was simultaneously measured using a laser interferometer system (SIOS MeβTechnik, GmbH, Type SP-S 120). Subsequently, strain was calculated from the electric-field displacement. The large signal piezoelectric coefficient was calculated using the maximum achievable strain (S_{max}) normalized by the maximum electric field (S_{max}/E_{max}), where E is unipolar. In-situ temperature dependent measurements of both polarisation and strain were carried out in the 25 to 175°C by the aforementioned procedure using a sample stage incorporating a heating element in close contact with the terminal electrodes. A heating rate of 1 °C/min and a holding time of 10 min was employed. The temperature accuracy of the measurements is ± 1 °C.

3-Results and Discussion

Fig. 1.a shows the room-temperature X-ray data for A-site donor Erbium doped ($Bi_{0.4-x/3}Na_{0.4-x/3}Sr_{0.2-x/3}Er_x)TiO_3$ (x=0, 0.015 and 0.02) ceramics. Within the detection limits of the technique the ceramics are single-phase. All reflections can be assigned to a pseudocubic single-phase perovskite. Basically, all the reflections are sharp and narrow and no obvious peak asymmetry due to distortions away from cubic symmetry can be detected. It is worth noting, that all reflections shifted towards higher 2θ with increasing Er content, this also becomes clear in the expanded view of Fig. 1.a, where the vertical dotted line is a guideline to the eye. This is also observed for the B-site acceptor Erbium doped $Bi_{0.4}Na_{0.4}Sr_{0.2}(Ti_{1-y}Er_y)O_3$ (y=0, 0.015 and 0.02) ceramics, as shown in Fig. 1.b. First, this compositional dependence of the peak positions indicates a reduction of lattice parameters and unit cell volumes in both doping mechanisms, as listed in Table I. Second, it also suggests

preferential A-site occupancy for Er. Indeed, based purely in ionic radii arguments, if Ti^{4+} was substituted by Er^{3+}, one would expect an increase of the unit cell volume, because Er^{3+} in six-fold coordination has an ionic radius of 0.89 Å[27], which is considerably larger than Ti^{4+} with an ionic radius of 0.605 Å.[27] The A-site preferential occupancy in $Bi_{0.4}Na_{0.4}Sr_{0.2}(Ti_{1-y}Er_y)O_3$ also suggests the occurrence of A-site vacancies due to volatilization of Bi^{3+} and/or Na^+, which then can accommodate Er^{3+}, but as it shown later a secondary phase is present in y=0.02 ceramics, which may also support a limited solubility of Er in the B-site.

At this stage, the formation of a core-shell microstructure as previously observed by Cho et al[25] in Fe-modified BNT-ST [$0.77(Bi_{0.5}Na_{0.5})TiO_3$-$0.23Sr(Ti_{1-x}Fe_x)O_3$] cannot be ruled out and transmission electron microscopy will be required to ascertain the sub-grain microstructure.

Raman spectra in Fig. 2 clearly show the crystal symmetry of all ceramics to deviate from perfect cubic crystal symmetry. This is also supported by a remarkable electroresponse, as discussed below. Indeed, the appearance of strong broad Raman modes offers clear evidence that their local crystal symmetry cannot be described by the cubic $Pm\bar{3}m$ space group, as previously discussed.[14, 28]. The Raman spectrum for BNT-20ST can be divide into three regions, corresponding to different types of lattice vibrations. These regions were assigned according to the work of Schütz et al[5]. Hence, modes in the < 150 cm^{-1} region can be associated with A-site vibrations, thus involving Bi, Na and Sr cations, whereas modes in 150-450 cm^{-1} region can be associated with Ti–O vibrations, in particular with the bond strength. Finally, high-frequency modes above 450 cm^{-1} have all been associated with TiO_6 vibrations, namely breathing and stretching of the oxygen octahedra. From Fig. 2, it becomes apparent that Er doping affects dramatically modes associated with Ti–O vibrations. Moreover, spectra for ceramics prepared according to ($Bi_{0.4-x/3}Na_{0.4-x/3}Sr_{0.2-}$

$_{x/3}Er_x)TiO_3$ and $Bi_{0.4}Na_{0.4}Sr_{0.2}(Ti_{1-x}Er_x)O_3$ formulas are remarkably identical, as shown in Fig. 2.a and 2.b, respectively. XRD analyses, Fig. 1, strongly suggested preferable A-site occupancy for Er, therefore the similarly between the two sets of Raman spectra, Fig. 2, may further corroborate this premise. Recently, Zannen et al[29] observed a similar impact on the Raman spectra of Er doping $Na_{0.5}Bi_{0.5}TiO_3$ ceramics. They discussed in detail the effects of Er incorporation on spectral features, in particular (i) increased broadness and shift towards lower frequencies of A-site related modes, (ii) shift and splitting of the mode centered at 270 cm^{-1} to higher frequencies and (iii) appearance of a new mode around 700 cm^{-1}, which in Fig. 2 is indicated by an asterisk. They suggested fluorescent effects caused by Er can give rise to some of the spectral changes, which therefore deserves further studies using lasers of different wavelengths.

All ceramics exhibited similar microstructures, encompassing grains with grain sizes varying from 4 to 8 μm, as illustrated in Fig. 3(a-e). For undoped $Bi_{0.4}Na_{0.4}Sr_{0.2}TiO_3$ ceramics the microstructure consists uniquely of cuboid-shaped grains, however upon doping a bimodal type microstructure encompassing rounded-shaped grains and larger (up to 8 μm) cuboid-shaped grains is observed, as illustrated in Fig. 3(b,d,e), for x=0.015, y=0.015 and y=0.02, respectively. Interestingly, $Bi_{0.4}Na_{0.4}Sr_{0.2}(Ti_{1-y}Er_y)O_3$ (y=0.02) ceramics contain a secondary phase with a plate-like morphology, as indicated by the arrows in Fig. 3.e. This secondary phase was not detected in the XRD analysis, mainly because its relative amount is below the detection limits of the technique, however its presence is consistent with Er^{3+} A-site preferential occupancy in this solid solution. Actually, Er^{3+} is noticeably known for its amphoteric doping behaviour in $BaTiO_3$ and other ferroelectric compounds[30]. Finally, at

this stage the chemical nature of this secondary phase remains unknown because its morphology makes EDX analysis challenging.

Hereafter, this work is focused on the single-phase A-site doped $(Bi_{0.4-x/3}Na_{0.4-x/3}Sr_{0.2-x/3}Er_x)TiO_3$ (x=0, 0.015 and 0.02) ceramics.

Temperature dependencies of the relative permittivity, ε_r, and dielectric loss, tan δ, for undoped BNT-20ST and 1.5 mol% Er-doped BNT-20ST ceramics (both unpoled and poled) are illustrated in Fig. 4. Both compositions exhibit two ε_r maxima around 150°C and 235°C (at 1 kHz). The lower temperature maximum is frequency dependent and shifts to higher temperatures with increasing temperatures (typical for a relaxor), whereas the high temperature maximum is relatively frequency independent. This dielectric response is like that reported by Weyland et al[31] for undoped BNT-25ST ceramics. A dramatic increase in tan δ is observed above 200°C in both unpoled and poled BNT-20ST ceramics, as shown in Fig. 4a and b, respectively. Er-doping enhances temperature stability of ε_r, which is accompanied with a reduction of the maximum permittivity from 3600 for undoped to 2800 for doped ceramics, as shown in Fig. 4.a and 4.c, respectively. Importantly, Er doping also reduces tan δ at high temperatures, corroborating an higher electrical resistivity, which is advantageous for high field and high temperature applications. The temperature dependence of ε_r and tan δ for poled ceramics was measured to gather some further insight into relaxor behaviour. The ε_r response remained relatively unchanged between unpoled and poled as shown in Fig. 4(a-d). In contrast, tan δ shows two distinctive responses. In undoped BNT-20ST, poling leads to the appearance of an extra low temperature loss peak, Fig. 4.b, in contrast with doped ceramics, Fig. 4.d. This can be rationalised as follows, undoped BNT-20ST is a non-ergodic relaxor at room temperature, meaning it transforms

irreversibly into a ferroelectric state under the application of a large electric field, for this reason the tan δ behaviour is different between the poled and unpoled. Indeed, as previously discussed by Weyland et al[31] this tan δ peak arises from a broad ferroelectric-to-relaxor transition. The A-substitution of 1.5 mol % Er in BNT-20ST is sufficient to induce a transition from a non-ergodic to an ergodic state, which is manifested by the absence of the low temperature loss peak in the tan δ behaviour of both unpoled and poled ceramics, as shown in Fig. 4c and d, respectively. Basically, the application of a sufficiently large electric field at room temperature can induce long-range ferroelectric order in an ergodic relaxor, however this is only stable under an electric field. Schutz et al[5] proposed that the loss of non-ergodicity in BNT-based materials is related to breaking of Bi–O hybridization. The non-ergodic to ergodic transition is also corroborated by the polarisation measurements presented below.

The piezoelectric coefficient, d_{33}, for undoped BNT-20ST and A-site Er-doped BNT-20ST was measured as 46 and 11 pC/N, respectively.

Room-temperature electric field-induced polarisation and strain in A-site Er-doped BNT-20ST ceramics measured at 1 Hz under an applied field of 60 kV/cm are illustrated in Fig. 5. These bipolar measurements show the slightly pinched ferroelectric hysteresis for undoped BNT-20ST ceramics to become increasingly slanted with increasing Er content, as shown in Fig. 5.a. This is also accompanied by the continuous evolution of the electric-field induced strain from a mostly butterfly-shaped into a sprout-shaped response for doped ceramics, as illustrated in Fig. 5.b. Basically, doping leads to a transition from a non-ergodic to an ergodic relaxor response, which is consistent with the permittivity measurements in Fig. 4. A similar behaviour was recently reported by Obilor et al[32] for Nb-doped BNT-BKT-BT ceramics.

Maximum achievable polarisations decrease continuously from ~38.8 μC/cm^2 for undoped BNT-20ST ceramics to ~35.4 μC/cm^2 and ~31.4 μC/cm^2 for 1.5 mol% and 2 mol% Er-doped ceramics, respectively. On the other hand, maximum achievable electric-field induced positive strains increase from 0.16% for BNT-20ST ceramics to 0.19% for 1.5 mol% Er-doped ceramics. With increasing Er-content this value decreases. It is also worth to mention that the negative strain observed in BNT-20ST ceramics is considerably smaller in Er-doped ceramics, as shown in Fig. 5.b. A recent work by Khatua et al[33] devoted to A-site doped BNT-6BT ceramics shows a similar drop in the maximum polarisation and modification to the electrostrain response. Negative strains arise from macrodomain switching in ferroelectric materials, therefore a reduction of the negative strain corroborates an evolution from non-ergodic to ergodic relaxor response. In contrast, the remnant strain slightly increases with increasing Er doping. The polarisation for undoped BNT-20ST ceramics is similar to that reported by Krauss et al[21], however the strain appears to be lower, whereas the coercive field appears greater. In comparison, the present strain results are similar to those reported by Jo et al[34], but the polarisation is larger and the coercive field smaller. This indicates that some level of softening may exist in samples prepared by Krauss et al[21]. Actually, the larger strain observed by Krauss et al[21] maybe associated to the presence of some minor doping impurity brought with the raw materials or from the milling process. For example, other researchers[35] have elegantly demonstrated that attrition milling $BaTiO_3$ with Y-stabilised zirconia media for 2-4 h is sufficient to create core-shell grain substructures, due to Y and Zr contamination. This non-intentional chemical modification impacts both electrical and dielectric properties. Based on the above, it can be suggested that for example 1.5 mol% of Er is sufficient to increase the strain from 0.16% to 0.19%.

Since only positive strains are usable in actuator devices, unipolar response of the aforementioned ceramics was measured, and the results are illustrated in Fig. 6. At room temperature, the maximum induced polarisation under an electric field of 60 kV/cm was measured for the 1.5% Er A-site doped sample, as illustrated on Fig. 6.a. Similarly, the maximum achievable strain under the same applied electric field is measured for the same composition, as illustrated in Fig. 6.b. Basically, the unipolar polarisation increases initially upon doping from 19 $\mu C/cm^2$ for undoped BNT-20ST to ~25 $\mu C/cm^2$ for the 1.5 mol% Er-doped composition, but subsequently decreasing to ~20 $\mu C/cm^2$ for 2 mol% Er-doped counterpart. In terms of strain a similar trend is observed for the field induced strain, which increases from ~0.16 % for the undoped to ~0.19 % for the 1.5 mol% Er-doped composition, and returns back to ~0.16 % for the 2 mol% Er-doped composition.

Two points are worth noting. First, the maximum bipolar polarisation is greater for the undoped BNT-20ST ceramics, however for unipolar measurements the greatest polarisation is observed for 1.5 mol% Er doped ceramics. This is a consequence of the larger bipolar remanent polarisation exhibit by undoped BNT-20ST ceramics, as shown in Fig. 5.a. A similar situation was observed by Humburg et al[36] in $(Ba_{1-x}Ca_x)(Zr_yTi_{1-y})O_3$ ceramics. Second, the degree of strain hysteresis calculared by the $\Delta S/S_{max}$ ratio, as the difference in the strain at $E_{max}/2$ normalized by S_{max} for undoped BNT-20STwas estimated as ~0.146. This value increases slightly to ~0.154 and ~0.183 for 1.5 and 2 mol% Er-doped compositions, respectively. In the past, it was observed that the maximum achievable strain is inversely proportional to stability of the induced ferroelectric order. Basically, a larger $\Delta S/S_{max}$ suggests a larger degree of instability in the field-induced ferroelectric order, and simultaneously larger electric field-induced strains. Here, $\Delta S/S_{max}$ the ratio value is the

largest for the 2 mol% Er-doped ceramics, however this higher degree of disorder does not result in the largest field-induced strain because those ceramics have the lowest maximum polarisation as shown in Fig. 6.a.

Finally, *In-situ* temperature dependent measurements between 25 and 175 °C measured at 1 Hz under an applied electric field of 40 kV/cm are illustrated in Fig. 7. The field-induced strain for undoped BNT-20ST ceramics evolves from a butterfly shaped-hysteresis at room-temperature into a parabolic shaped response, as shown in Fig. 7.a. This evolution is accompanied by gradual disappearance of negative strain at high temperatures, but also by a large variation of the maximum achievable strain. The largest induced strain is measured at 100°C, when the negative strain completely disappears and the butterfly-shaped response is replaced by a sprout-shaped response. In contrast, 1.5 mol% Er-doped composition showed a rather parabolic response across the entire temperature range, as illustrated in Fig. 7.b. Moreover, in the 25 to 150°C temperature range, the maximum achievable strain remains within the 0.15 to 0.17% range, only dropping to 0.12% at 175°C. A similar response (not shown) was observed for 2 mol% Er-doped composition. In the temperature range that undoped BNT-20ST behaves as a non-ergodic relaxor, the application an electric field leads to induced long-range ordered ferroelectricity, which remains stable in the timescale of the measurements. With increasing temperature, thermal fluctuations will prevent the existence of long-range ordering at zero field, as shown in Fig. 7.a.

The impact of A-site Er-doping on the temperature stability of the field induced strain of BNT-20ST is summarised in Fig. 8. An enhancement of both the maximum achievable electric-field induced strain and its temperature stability becomes clearly evident for 1.5

mol% Er-doped ceramics. In undoped BNT-20ST ceramics, field-induced strain under an electric field of 40 kV/cm increases from 0.09% at room-temperature to nearly 0.18% at 100 °C and subsequently decreases to 0.08% at 175°C. In contrast, 1.5 mol% Er-doped ceramics exhibit a room-temperature strain as large as 0.15% which increases to slightly over 0.17% at 100°C. Above, this temperature it also decreases, but again less dramatically than the undoped ceramic counterparts. The 2 mol% Er-doped ceramics also show enhanced thermal stability, however at the expense of the maximum achievable strain, which at room-temperature is around 0.11%. Nevertheless, within the 25-155°C temperature range the maximum achievable strain for 1.5 mol% Er-doped ceramics does not vary more than 20%.

4-Conclusions

XRD analyses show Er to occupy preferentially the A-site in $0.80Bi_{0.5}Na_{0.5}TiO_3$-$0.20SrTiO_3$ (BNT-20ST) perovskite-structured ceramics, as indicated by the reduction of the unit cell volume. Doping lead to a transition from a non-ergodic to ergodic relaxor behaviour. Moreover, the A-site Er doped ceramics exhibited a moderate enhancement of the electric-field induced strain and reduced dielectric losses at high temperature. The maximum achievable unipolar electric-field induced strain under an applied field of 60 kV/cm increases from 0.17 % for undoped BNT-20ST to 0.19% for the 1.5 mol% Er-doped ceramic, but decreases to 0.16 % for 2 mol% Er, suggesting an optimum minor doping level lower than 2 mol% Er. On the other hand, *In-situ* temperature dependent strain measurements between 20 and 175 °C, revealed a dramatic improvement of the temperature stability properties for 1.5 mol% Er-doped ceramics, to less than 20% variation.

Acknowledgements

K.M. acknowledges the UoS for financial support during her studies at SHU. AF acknowledges SHU Strategic Research Investment Fund. DW acknowledges financial support from EPSRC through the grant EP/N010493/1-SYnthesizing 3D METAmaterials for RF, microwave and THz applications (SYMETA).

References

[1] J. Roedel, K.G. Webber, R. Dittmer, W. Jo, M. Kimura, D. Damjanovic, Journal of the European Ceramic Society 35 (2015) 1659-1681.
[2] H. Zhang, P. Xu, E. Patterson, J. Zang, S. Jiang, J. Roedel, Journal of the European Ceramic Society 35 (2015) 2501-2512.
[3] S. Zhang, A. Kounga, E. Aulbach, H. Ehrenberg, J. Rodel, Applied Physics Letters 91 (2007).
[4] S.T. Zhang, A.B. Kounga, W. Jo, C. Jamin, K. Seifert, T. Granzow, J. Rodel, D. Damjanovic, Advanced Materials 21 (2009) 4716-+.
[5] D. Schutz, M. Deluca, W. Krauss, A. Feteira, T. Jackson, K. Reichmann, Advanced Functional Materials 22 (2012) 2285-2294.
[6] K. Reichmann, A. Feteira, M. Li, Materials 8 (2015) 8467-8495.
[7] W. Krauss, D. Schutz, M. Naderer, D. Orosel, K. Reichmann, Journal of the European Ceramic Society 31 (2011) 1857-1860.
[8] H. Xie, Y.Y. Zhao, J.W. Xu, L. Yang, C.R. Zhou, H.B. Zhang, X.W. Zhang, W. Qiu, H. Wang, Journal of Alloys and Compounds 743 (2018) 73-82.
[9] X.R. Jia, J.J. Zhang, H.J. Xing, J.Y. Wang, P. Zheng, F. Wen, Journal of Alloys and Compounds 741 (2018) 7-13.
[10] A. Khesro, D.W. Wang, F. Hussain, D.C. Sinclair, A. Feteira, I.M. Reaney, Applied Physics Letters 109 (2016) 142907.
[11] Y.P. Guo, K. Kakimoto, H. Ohsato, Applied Physics Letters 85 (2004) 4121-4123.
[12] Y.P. Guo, K. Kakimoto, H. Ohsato, Solid State Communications 129 (2004) 279-284.
[13] D.W. Wang, F. Hussain, A. Khesro, A. Feteira, Y. Tian, Q.L. Zhao, I.M. Reaney, Journal of the American Ceramic Society 100 (2017) 627-637.
[14] C. Pascual-Gonzalez, G. Schileo, A. Khesro, I. Sterianou, D. Wang, I.M. Reaney, A. Feteira, Journal of Materials Chemistry C (2017) 1990-1996.
[15] K. Matsumoto, Y. Hiruma, H. Nagata, T. Takenaka, Ceramics International 34 (2008) 787-791.
[16] X. Lv, Z.Y. Li, J.G. Wu, D.Q. Xiao, J.G. Zhu, Acs Applied Materials & Interfaces 8 (2016) 30304-30311.
[17] W. Krauss, D. Schutz, F.A. Mautner, A. Feteira, K. Reichmann, Journal of the European Ceramic Society 30 (2010) 1827-1832.
[18] H. Simons, J. Daniels, W. Jo, R. Dittmer, A. Studer, M. Avdeev, J. Roedel, M. Hoffman, Applied Physics Letters 98 (2011).
[19] X. Liu, J. Shi, F.Y. Zhu, H.L. Du, T.Y. Li, X.C. Liu, H. Lu, Journal of Materiomics 4 (2018) 202-207.
[20] Y. Hiruma, Y. Imai, Y. Watanabe, H. Nagata, T. Takenaka, Applied Physics Letters 92 (2008).
[21] W. Krauss, D. Schuetz, F.A. Mautner, A. Feteira, K. Reichmann, Journal of the European Ceramic Society 30 (2010) 1827-1832.
[22] M. Acosta, W. Jo, J. Rodel, Journal of the American Ceramic Society 97 (2014) 1937-1943.
[23] S. Kim, H. Choi, S. Han, J.S. Park, M.H. Lee, T.K. Song, M.-H. Kim, D. Do, W.-J. Kim, Journal of the European Ceramic Society 37 (2017) 1379-1386.

[24] J. Koruza, V. Rojas, L. Molina-Luna, U. Kunz, M. Duerrschnabel, H.J. Kleebe, M. Acosta, Journal of the European Ceramic Society 36 (2016) 1009-1016.
[25] J.-H. Cho, J.-S. Park, S.-W. Kim, Y.-H. Jeong, J.-S. Yun, W.-I. Park, Y.-W. Hong, J.-H. Paik, Journal of the European Ceramic Society 37 (2017) 3313-3318.
[26] Z. Rashad, A. Feteira, Materials Letters doi.org/10.1016/j.matlet.2018.1003.1183.
[27] R.D. Shannon, Acta Crystallographica Section A 32 (1976) 751-767.
[28] A. Feteira, D.C. Sinclair, J. Kreisel, Journal of the American Ceramic Society 93 (2010) 4174-4181.
[29] M. Zannen, M. Dietze, H. Khemakhem, A. Kabadou, M. Es-Souni, Ceramics International 40 (2014) 13461-13469.
[30] T.D. Dunbar, W.L. Warren, B.A. Tuttle, C.A. Randall, Y. Tsur, Journal of Physical Chemistry B 108 (2004) 908-917.
[31] F. Weyland, M. Acosta, M. Vogler, Y. Ehara, J. Rodel, N. Novak, Journal of Materials Science 53 (2018) 9393-9400.
[32] U. Obilor, C. Pascual-Gonzalez, S. Murakami, I.M. Reaney, A. Feteira, Materials Research Bulletin 97 (2018) 385-392.
[33] D.K. Khatua, A. Agarwal, A. Mishra, G. Das Adhikary, A. Senyshyn, R. Ranjan, Journal of Applied Physics 124 (2018) 10.
[34] S. Jo, C.-H. Hong, D.S. Kim, H.-W. Kang, C.W. Ahn, H.-G. Lee, S. Nahm, W. Jo, S.H. Han, Sensors and Actuators A: Physical 258 (2017) 201-207.
[35] O.P. Thakur, A. Feteira, B. Kundys, D.C. Sinclair, Journal of the European Ceramic Society 27 (2007) 2577-2589.
[36] H.I. Humburg, M. Acosta, W. Jo, K.G. Webber, J. Rödel, Journal of the European Ceramic Society 35 (2015) 1209-1217.

List of Figures

Fig. 1 Room-temperature X-ray diffraction data for (a) $(Bi_{0.4-x/3}Na_{0.4-x/3}Sr_{0.2-x/3}Er_x)TiO_3$ (x=0, 0.015 and 0.02) and (b) $Bi_{0.4}Na_{0.4}Sr_{0.2}(Ti_{1-y}Er_y)O_3$ (x=0, 0.015 and 0.02) ceramics fired at 1250°C. The vertical dotted lines in the expanded views are provided as guidelines to the eye.

Fig. 2 Room-temperature Raman spectra for (a) $(Bi_{0.4-x/3}Na_{0.4-x/3}Sr_{0.2-x/3}Er_x)TiO_3$ (x=0, 0.015 and 0.02) and (b) $Bi_{0.4}Na_{0.4}Sr_{0.2}(Ti_{1-y}Er_y)O_3$ (x=0, 0.015 and 0.02) ceramics fired at 1250°C.

Fig. 3 Ceramic microstructures of $(Bi_{0.4-x/3}Na_{0.4-x/3}Sr_{0.2-x/3}Er_x)TiO_3$ (a) x=0, (b) x=0.015 and (c) x=0.02 and $Bi_{0.4}Na_{0.4}Sr_{0.2}(Ti_{1-y}Er_y)O_3$ (d) y=0.015 and (e) y=0.02 ceramics fired at 1250°C.

Fig. 4 Temperature dependence of the relative permittivity, ε_r, and dielectric loss, tan δ, for (a) unpoled$(Bi_{0.4}Na_{0.4}Sr_{0.2})TiO_3$, (b) poled $(Bi_{0.4}Na_{0.4}Sr_{0.2})TiO_3$, (c) unpoled $(Bi_{0.395}Na_{0.395}Sr_{0.195}Er_{0.015})TiO_3$ and (d) poled $(Bi_{0.395}Na_{0.395}Sr_{0.195}Er_{0.015})TiO_3$

Fig. 5 Room-temperature bipolar measurements of electric field-induced (a) polarisation and (b) strain for $(Bi_{0.4-x/3}Na_{0.4-x/3}Sr_{0.2-x/3}Er_x)TiO_3$ (x=0, 0.015 and 0.02) ceramics.

Fig. 6 Room-temperature unipolar measurements of electric field-induced (a) polarisation and (b) strain for $(Bi_{0.4-x/3}Na_{0.4-x/3}Sr_{0.2-x/3}Er_x)TiO_3$ (x=0, 0.015 and 0.02) ceramics.

Fig. 7 *In-situ* temperature dependent strain vs electric field measurements for $(Bi_{0.4-x/3}Na_{0.4-x/3}Sr_{0.2-x/3}Er_x)TiO_3$ (a) x=0 and (b) x=0.015 ceramics.

Fig. 8 Temperature dependence of the electric field induced strain for $(Bi_{0.4-x/3}Na_{0.4-x/3}Sr_{0.2-x/3}Er_x)TiO_3$ (x=0, 0.015 and 0.02) ceramics under an applied field of 40 kV/cm.

List of Tables

Table I. Refined lattice parameters for $(Bi_{0.4-x/3}Na_{0.4-x/3}Sr_{0.2-x/3}Er_x)TiO_3$ (x=0, 0.015 and 0.02) and $Bi_{0.4}Na_{0.4}Sr_{0.2}(Ti_{1-y}Er_y)O_3$ (x=0, 0.015 and 0.02) ceramics fired at 1250°C.

Table I

	A-site		B-site	
mol% Er	A (Å)	Vol ($Å^3$)	A (Å)	Vol ($Å^3$)
0	3.8963(4)	59.149(9)	3.8963(4)	59.149(9)
1.5	3.8919(5)	58.949(5)	3.89017(15)	58.872(6)
2	3.8894(5)	58.839(12)	3.8895(6)	58.840(17)

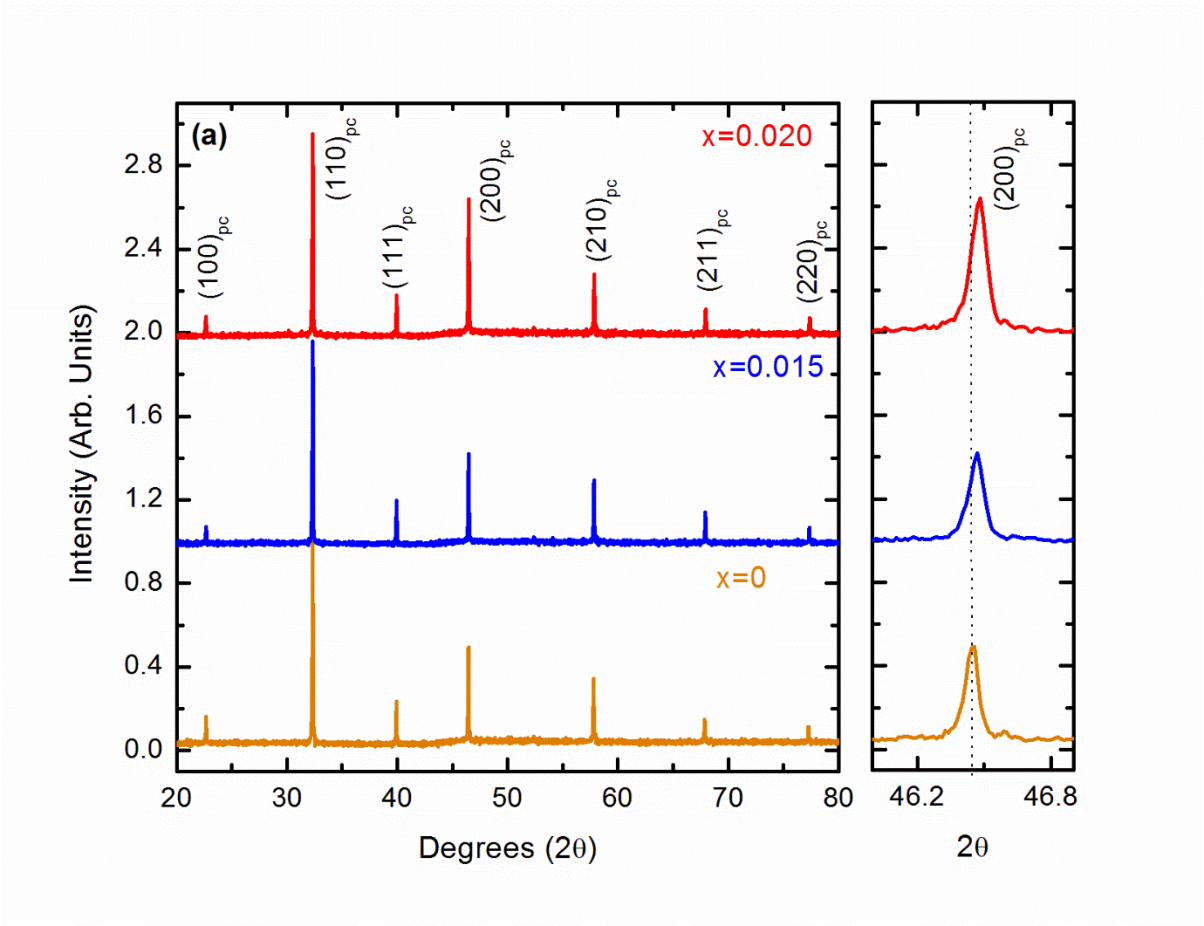
(a)
x=0.020
x=0.015
x=0
(100)pc
(110)pc
(111)pc
(200)pc
(210)pc
(211)pc
(220)pc
Intensity (Arb. Units)
Degrees (2θ)
2θ
0.0
0.4
0.8
1.2
1.6
2.0
2.4
2.8
20
30
40
50
60
70
80
46.2
46.8

Figure 1a

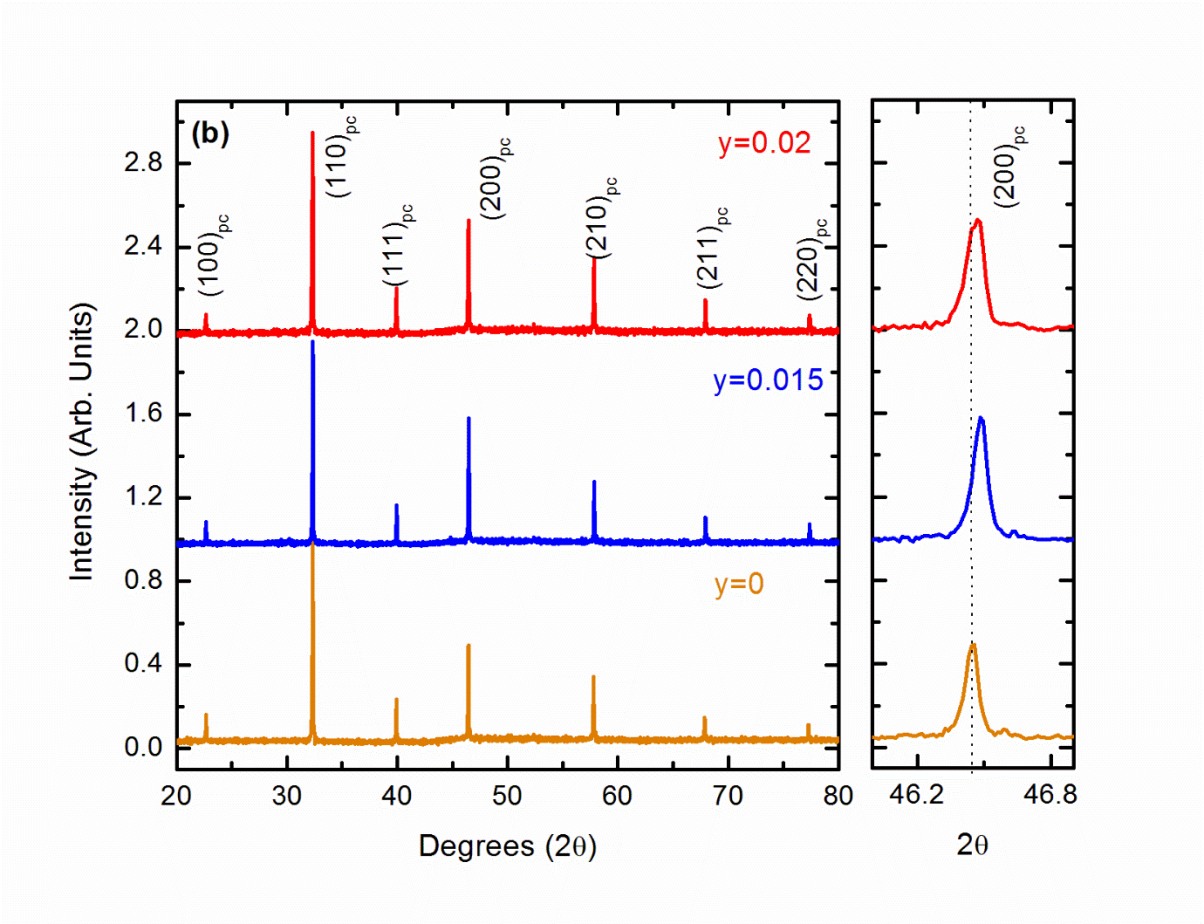
(b)
y=0.02
y=0.015
y=0
(100)pc
(110)pc
(111)pc
(200)pc
(210)pc
(211)pc
(220)pc
(200)pc
Intensity (Arb. Units)
Degrees (2θ)
2θ
0.0
0.4
0.8
1.2
1.6
2.0
2.4
2.8
20
30
40
50
60
70
80
46.2
46.8

Figure 1.b

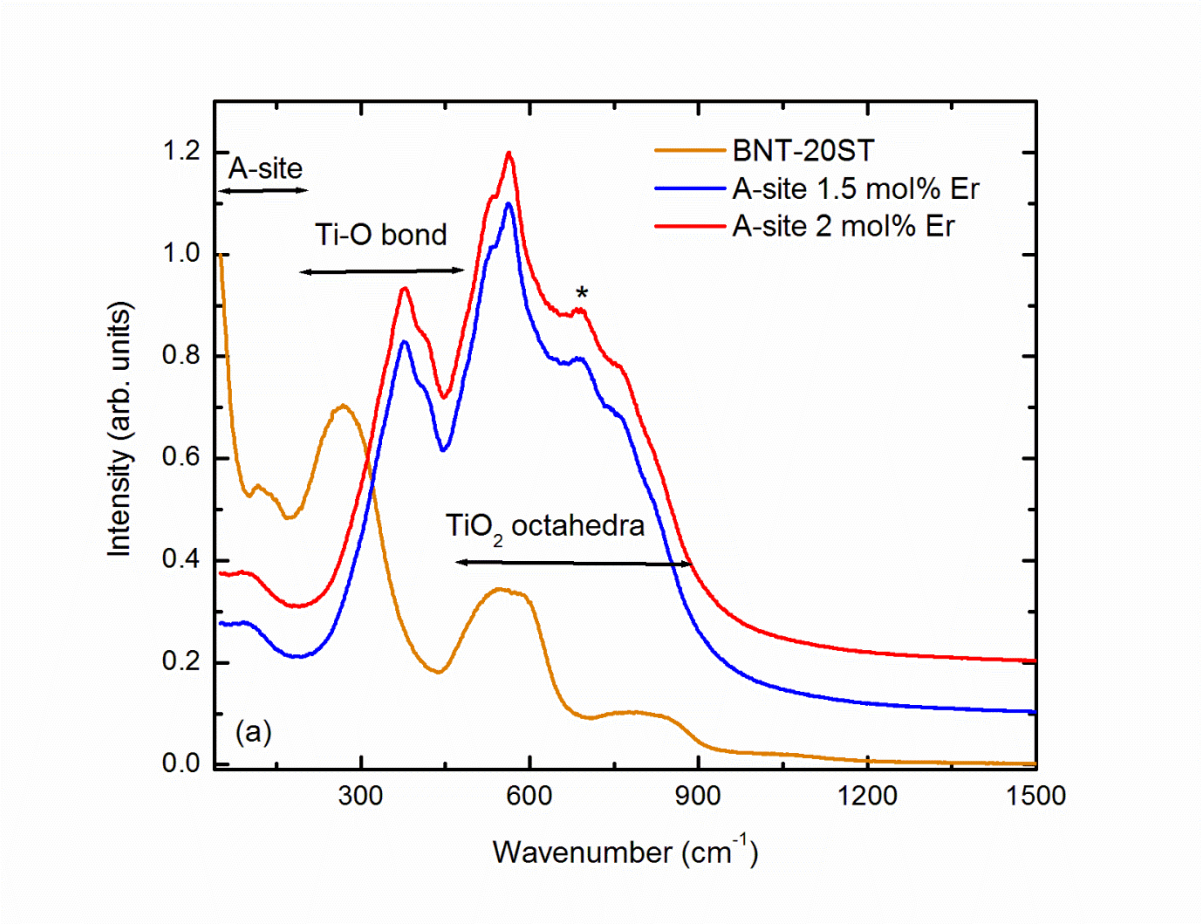
A-site
Ti-O bond
TiO2 octahedra
*
(a)
BNT-20ST
A-site 1.5 mol% Er
A-site 2 mol% Er
Intensity (arb. units)
Wavenumber (cm-1)
0.0
0.2
0.4
0.6
0.8
1.0
1.2
300
600
900
1200
1500

Figure 2a

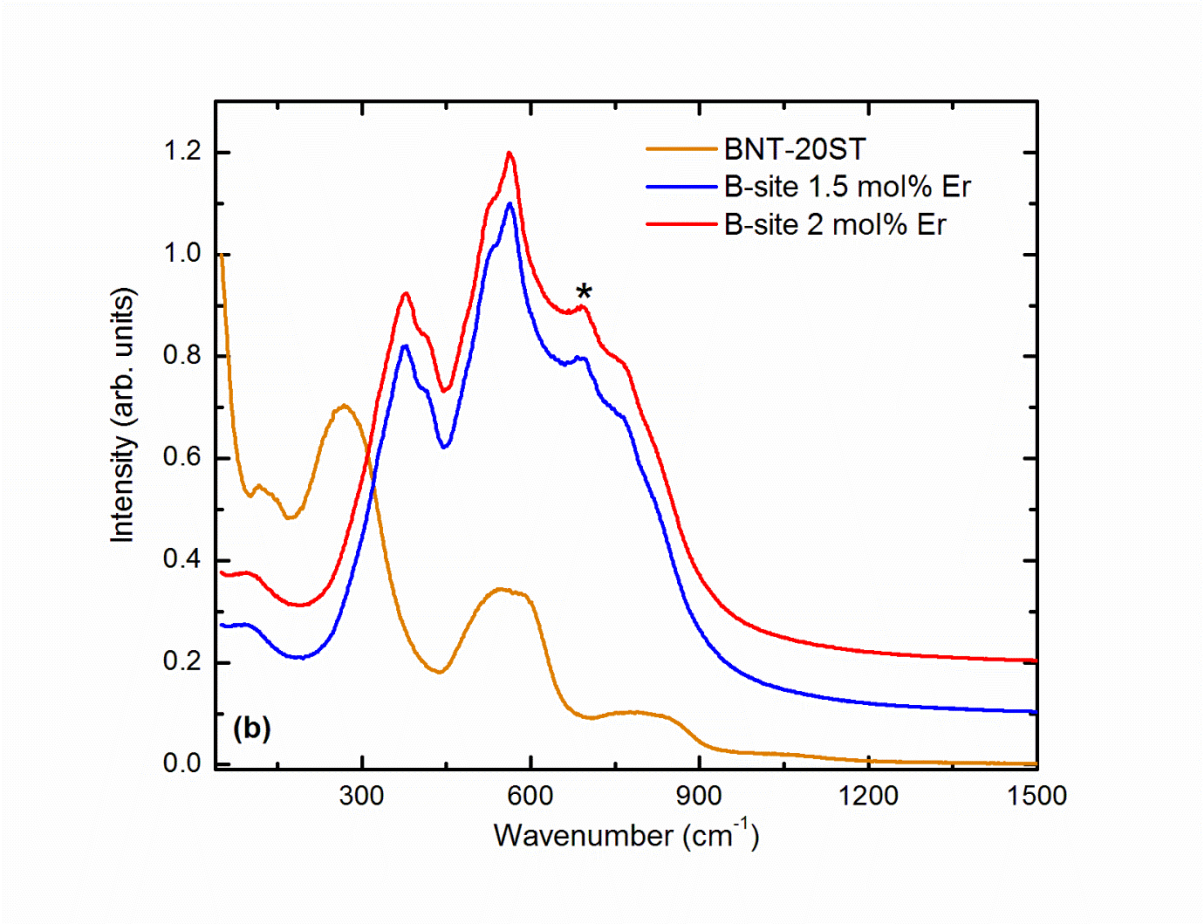
BNT-20ST
B-site 1.5 mol% Er
B-site 2 mol% Er
*
(b)
Intensity (arb. units)
Wavenumber (cm-1)
0.0
0.2
0.4
0.6
0.8
1.0
1.2
300
600
900
1200
1500

Figure 2b

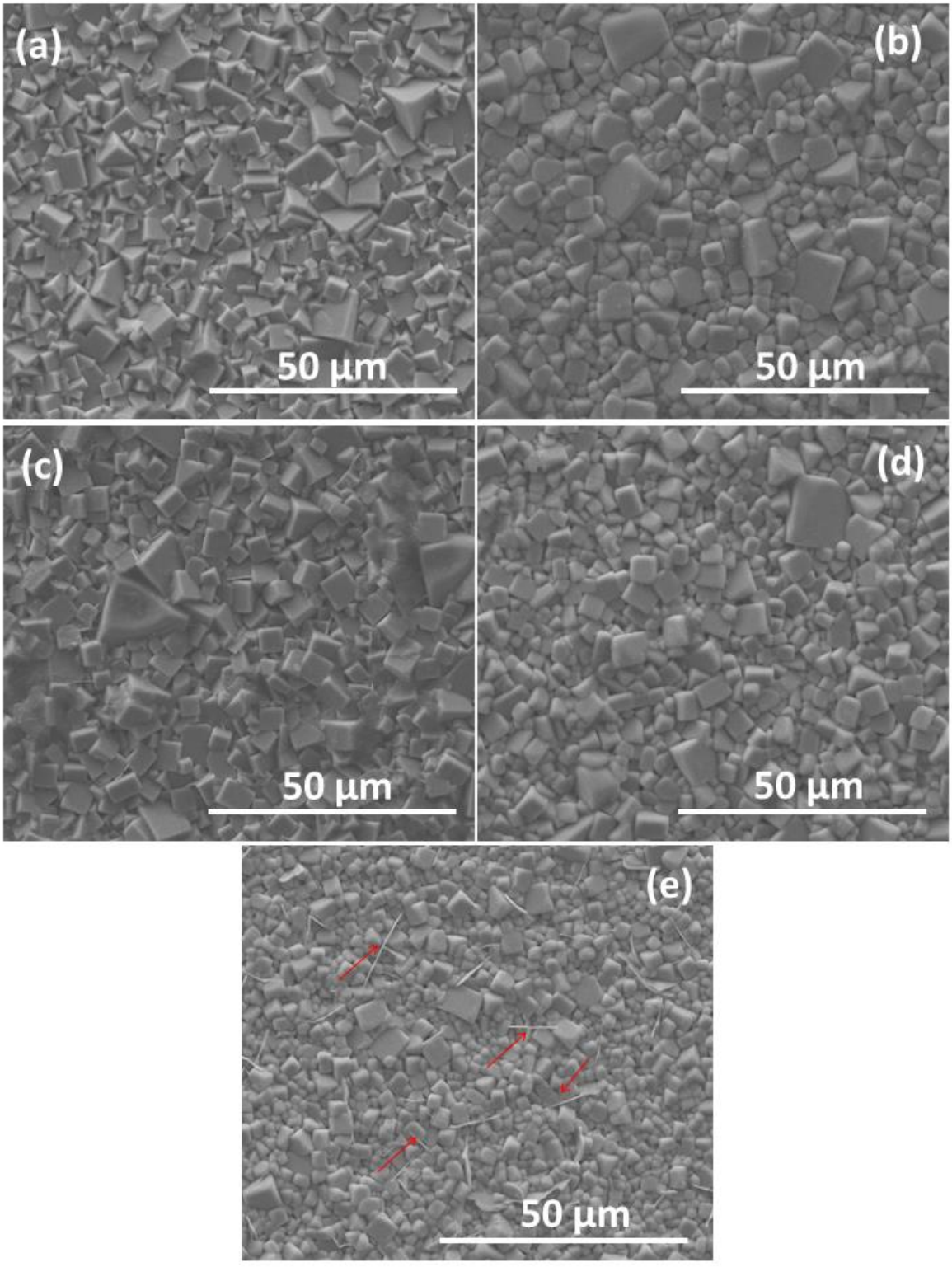

Figure 3

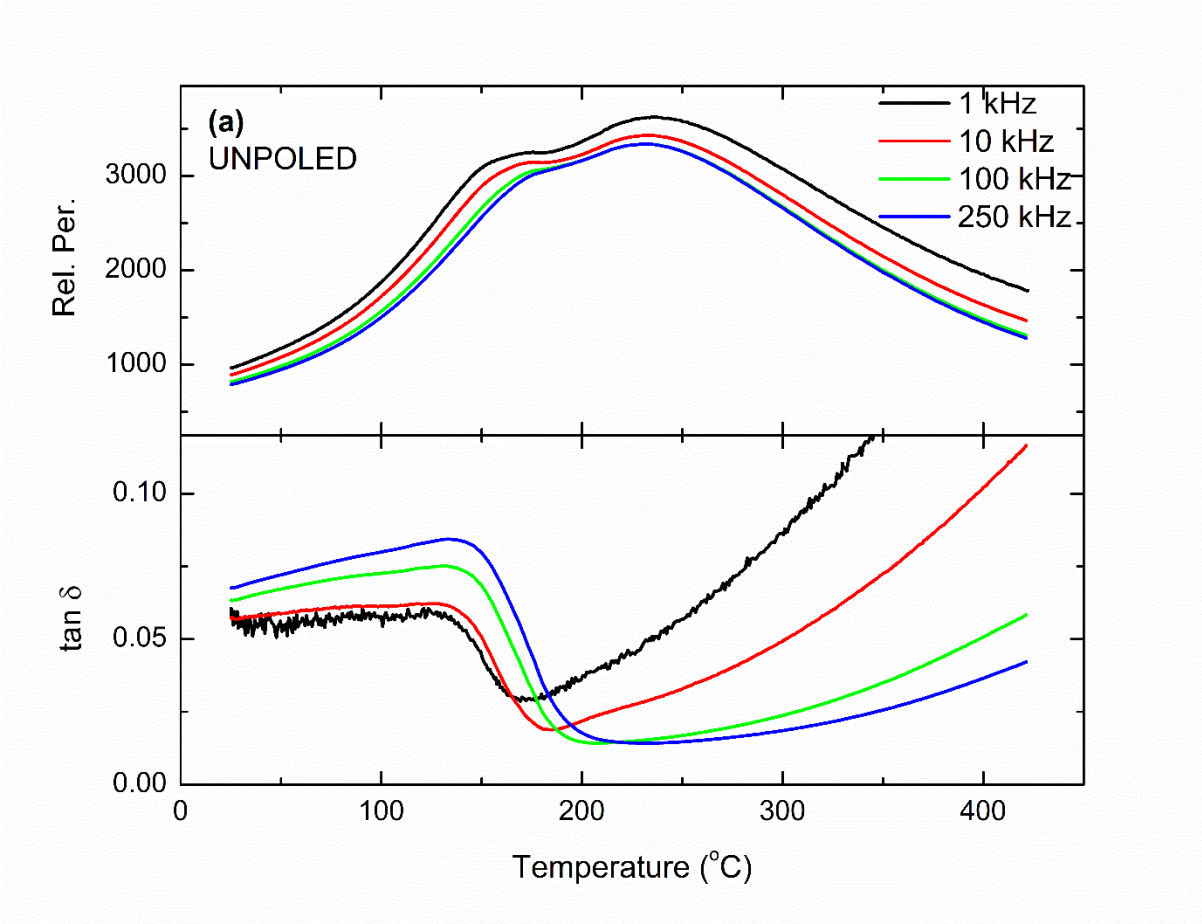
(a)
UNPOLED
1 kHz
10 kHz
100 kHz
250 kHz
Rel. Per.
3000
2000
1000
tan δ
0.10
0.05
0.00
0
100
200
300
400
Temperature (°C)

Fig. 4a

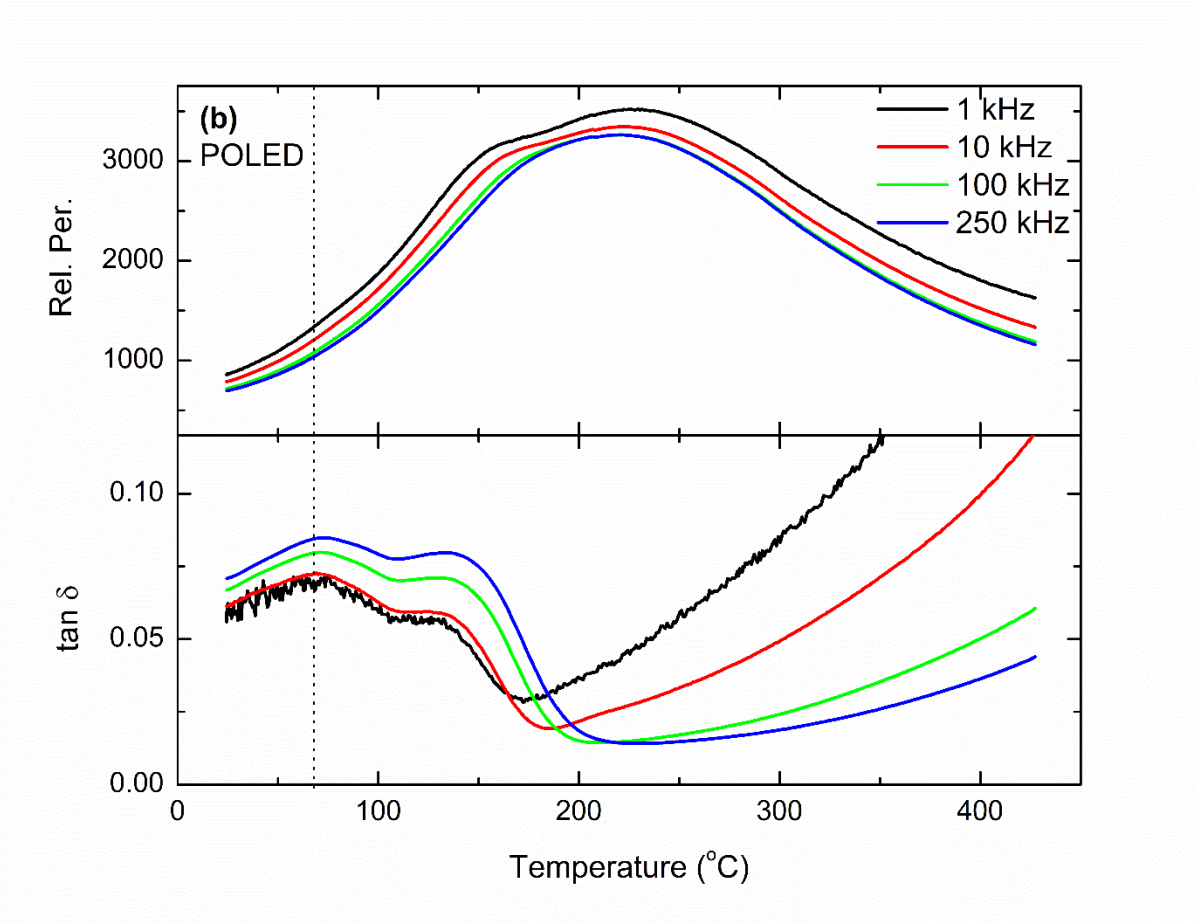
(b)
POLED
1 kHz
10 kHz
100 kHz
250 kHz
Rel. Per.
3000
2000
1000
tan δ
0.10
0.05
0.00
0
100
200
300
400
Temperature (°C)

Fig. 4.b

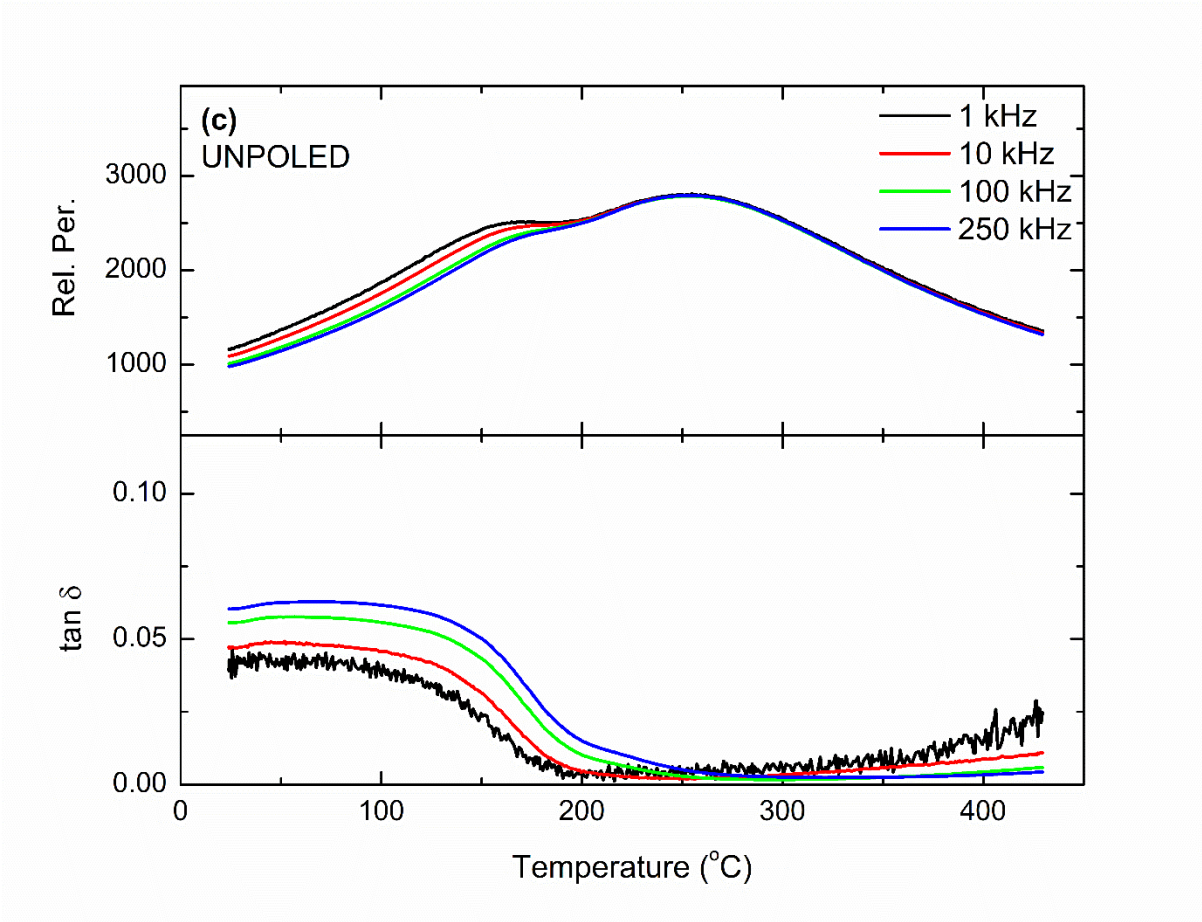
(c)
UNPOLED
1 kHz
10 kHz
100 kHz
250 kHz
Rel. Per.
3000
2000
1000
tan δ
0.10
0.05
0.00
0
100
200
300
400
Temperature (°C)

Fig. 4c

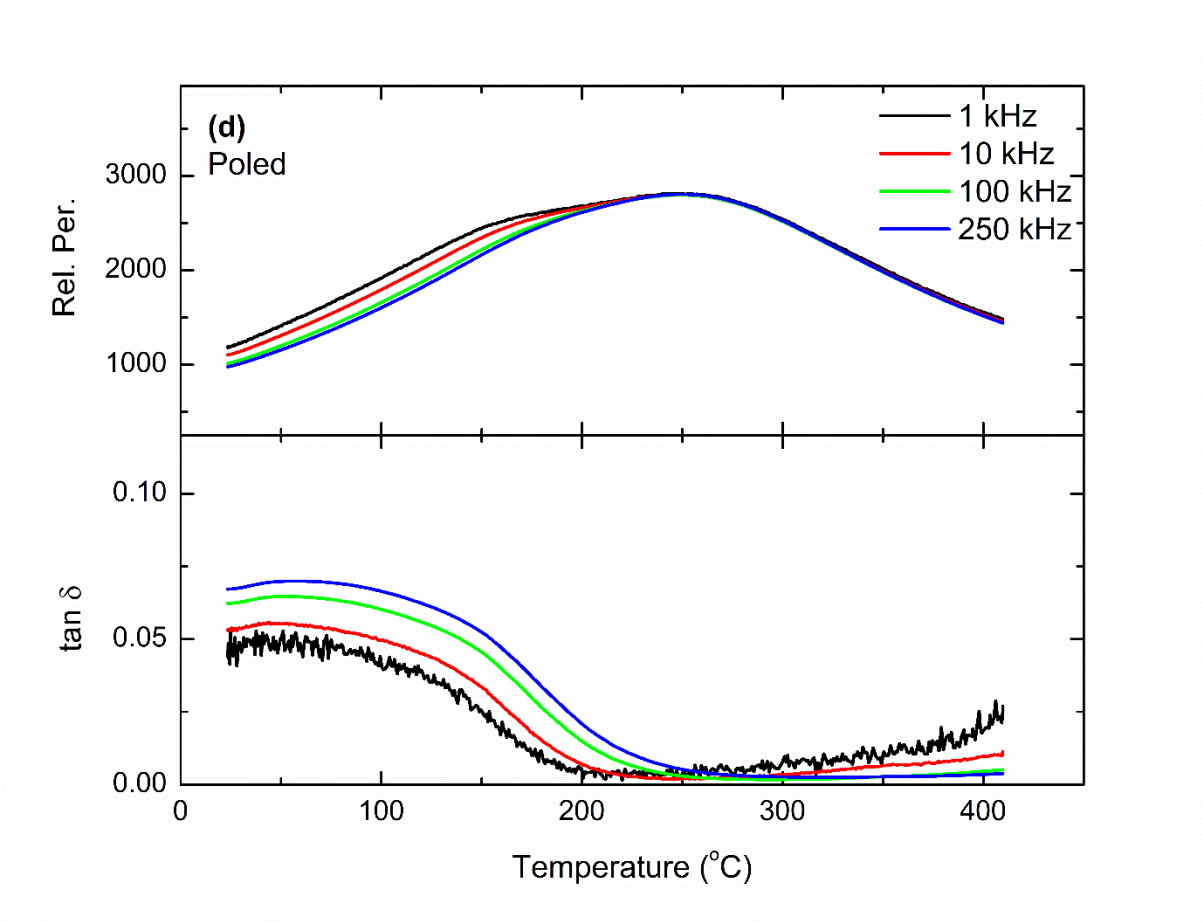
(d)
Poled
1 kHz
10 kHz
100 kHz
250 kHz
Rel. Per.
3000
2000
1000
tan δ
0.10
0.05
0.00
0
100
200
300
400
Temperature (°C)

Fig. 4d

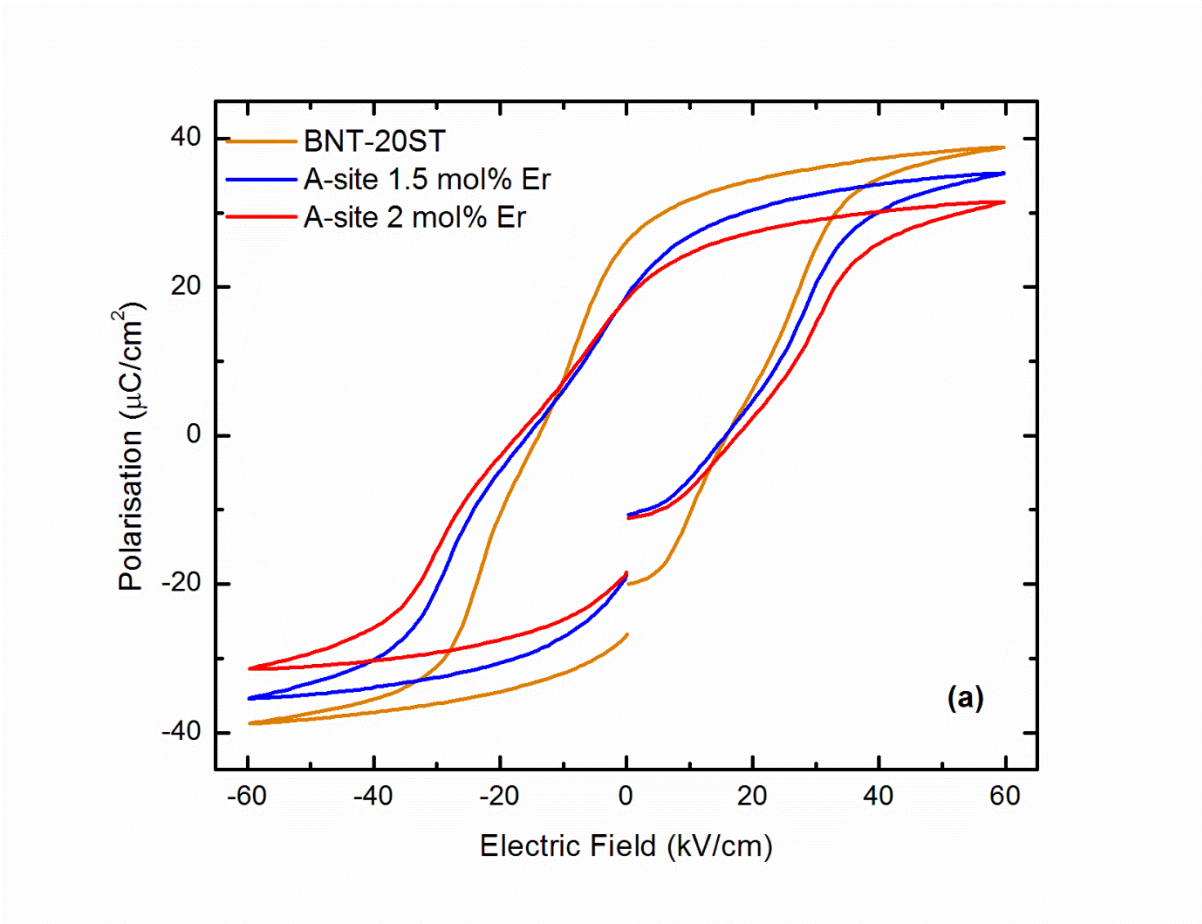
BNT-20ST
A-site 1.5 mol% Er
A-site 2 mol% Er
Polarisation (μC/cm²)
Electric Field (kV/cm)
(a)
40
20
0
-20
-40
-60
-40
-20
0
20
40
60

Figure 5a

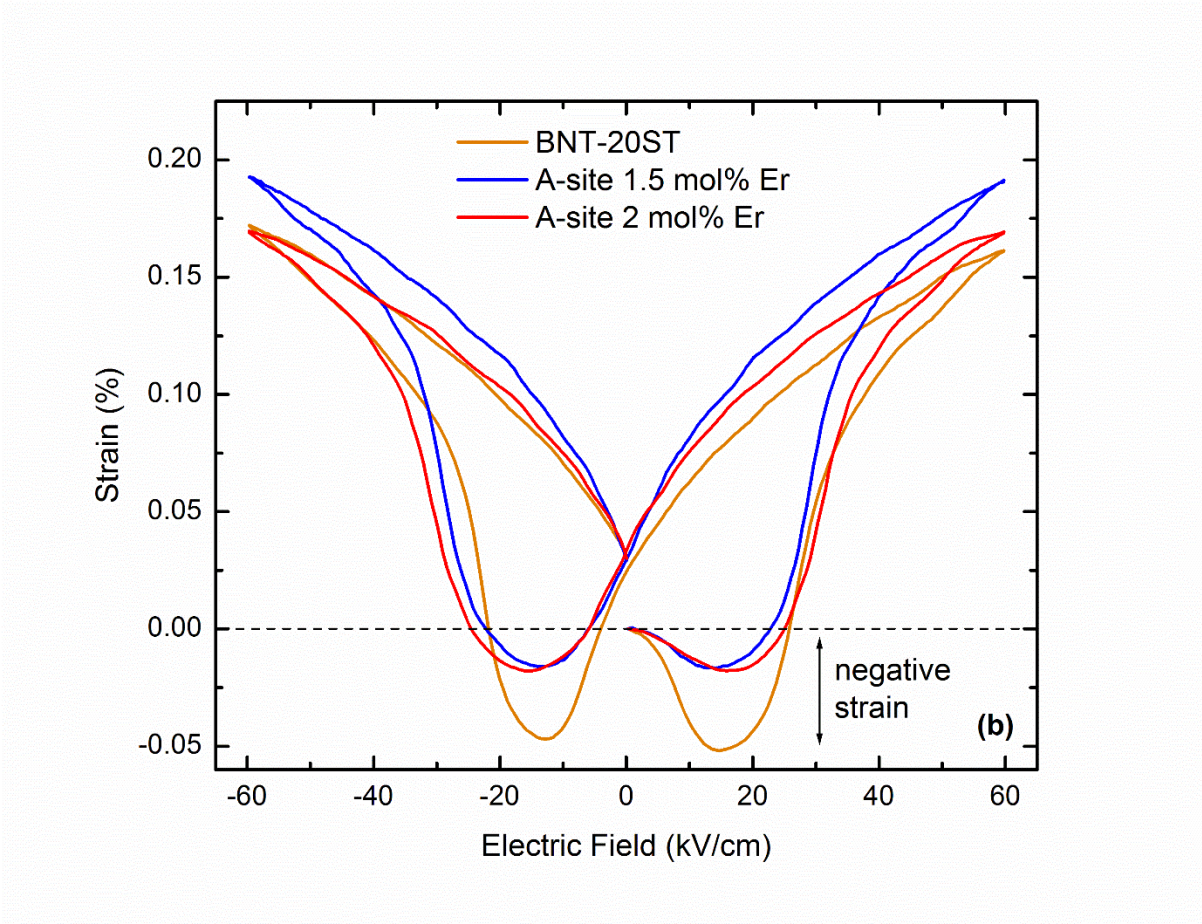
BNT-20ST
A-site 1.5 mol% Er
A-site 2 mol% Er
Strain (%)
0.20
0.15
0.10
0.05
0.00
-0.05
-60
-40
-20
0
20
40
60
Electric Field (kV/cm)
negative
strain
(b)

Figure 5b

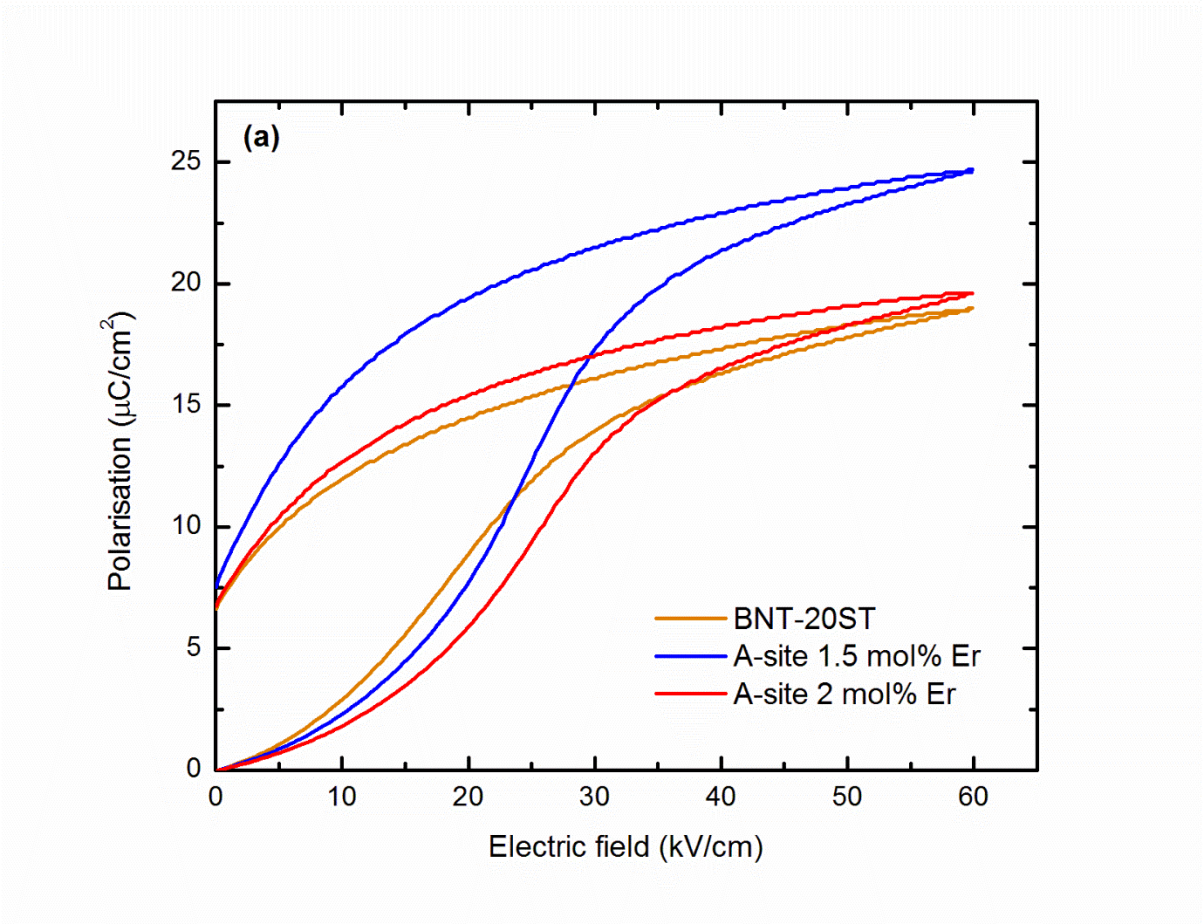
(a)
Polarisation (μC/cm²)
Electric field (kV/cm)
0
5
10
15
20
25
0
10
20
30
40
50
60
BNT-20ST
A-site 1.5 mol% Er
A-site 2 mol% Er

Figure 64a

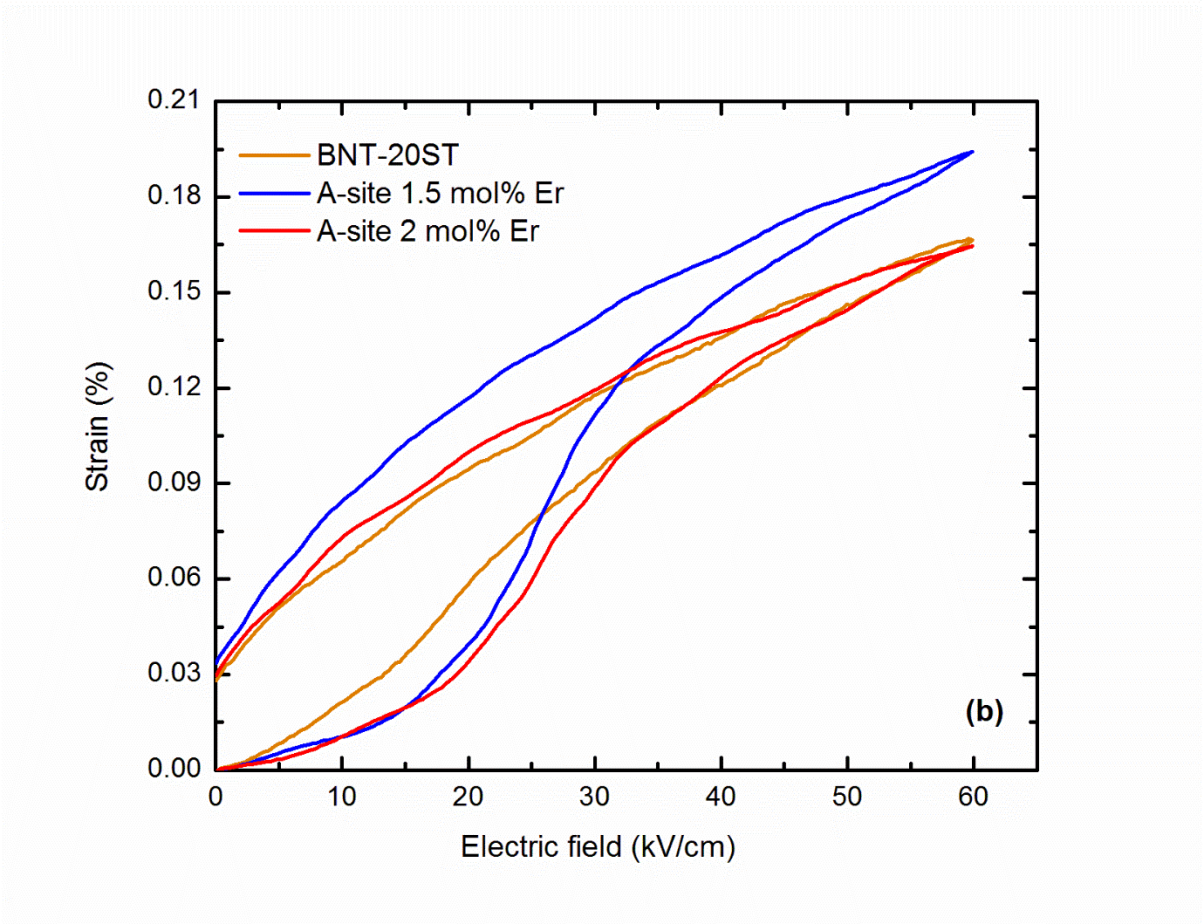
BNT-20ST
A-site 1.5 mol% Er
A-site 2 mol% Er
Strain (%)
Electric field (kV/cm)
(b)
0.00
0.03
0.06
0.09
0.12
0.15
0.18
0.21
0
10
20
30
40
50
60

Figure 6b

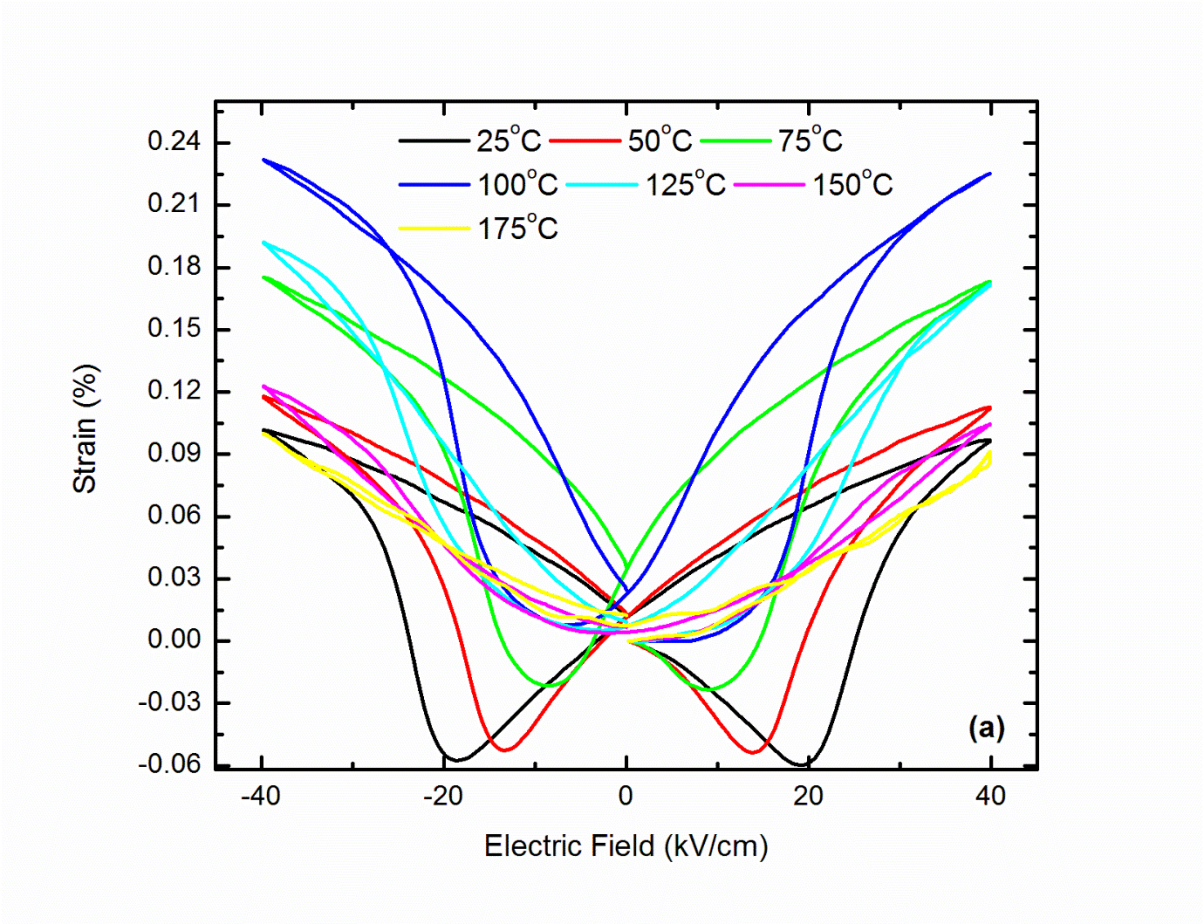
25°C
50°C
75°C
100°C
125°C
150°C
175°C
Strain (%)
0.24
0.21
0.18
0.15
0.12
0.09
0.06
0.03
0.00
-0.03
-0.06
-40
-20
0
20
40
Electric Field (kV/cm)
(a)

Figure 7a

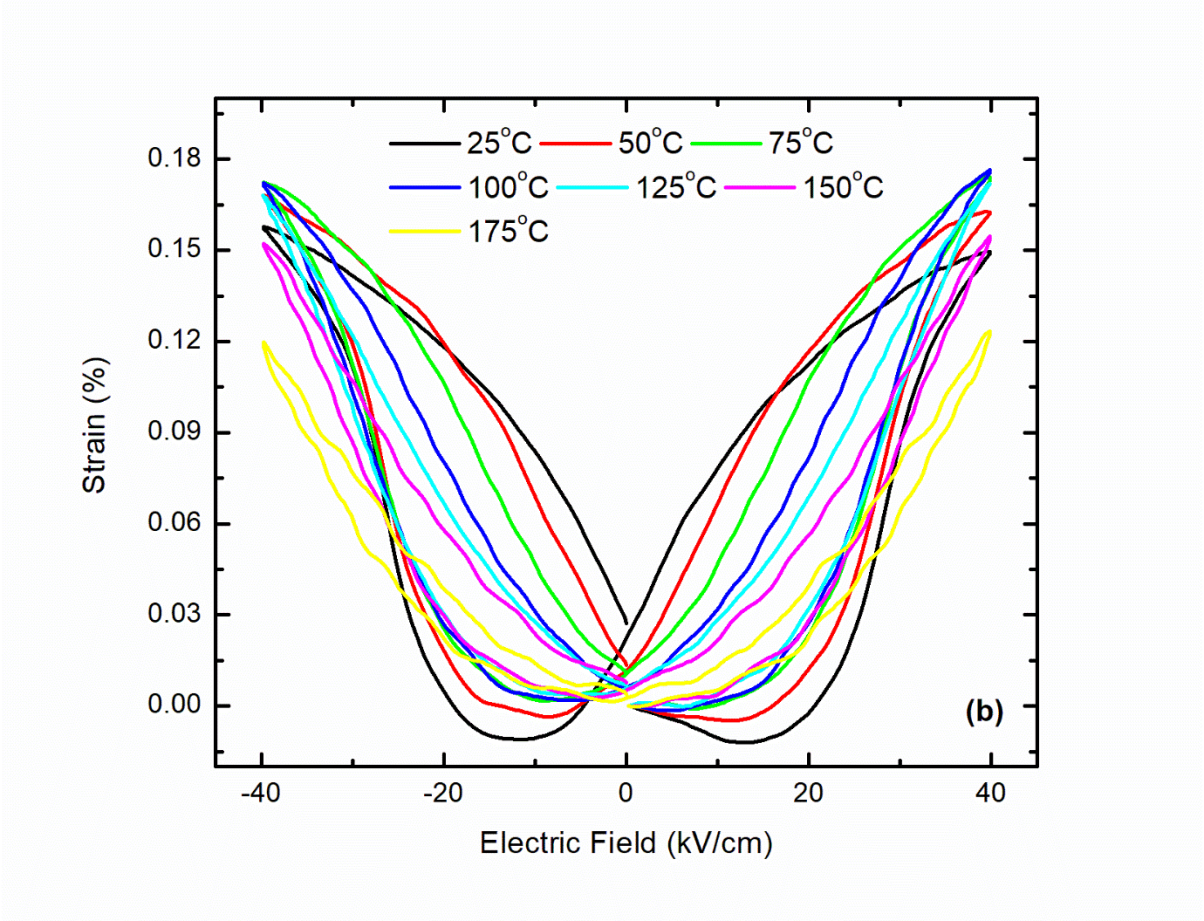
25°C
50°C
75°C
100°C
125°C
150°C
175°C
Strain (%)
0.18
0.15
0.12
0.09
0.06
0.03
0.00
-40
-20
0
20
40
Electric Field (kV/cm)
(b)

Figure 7b

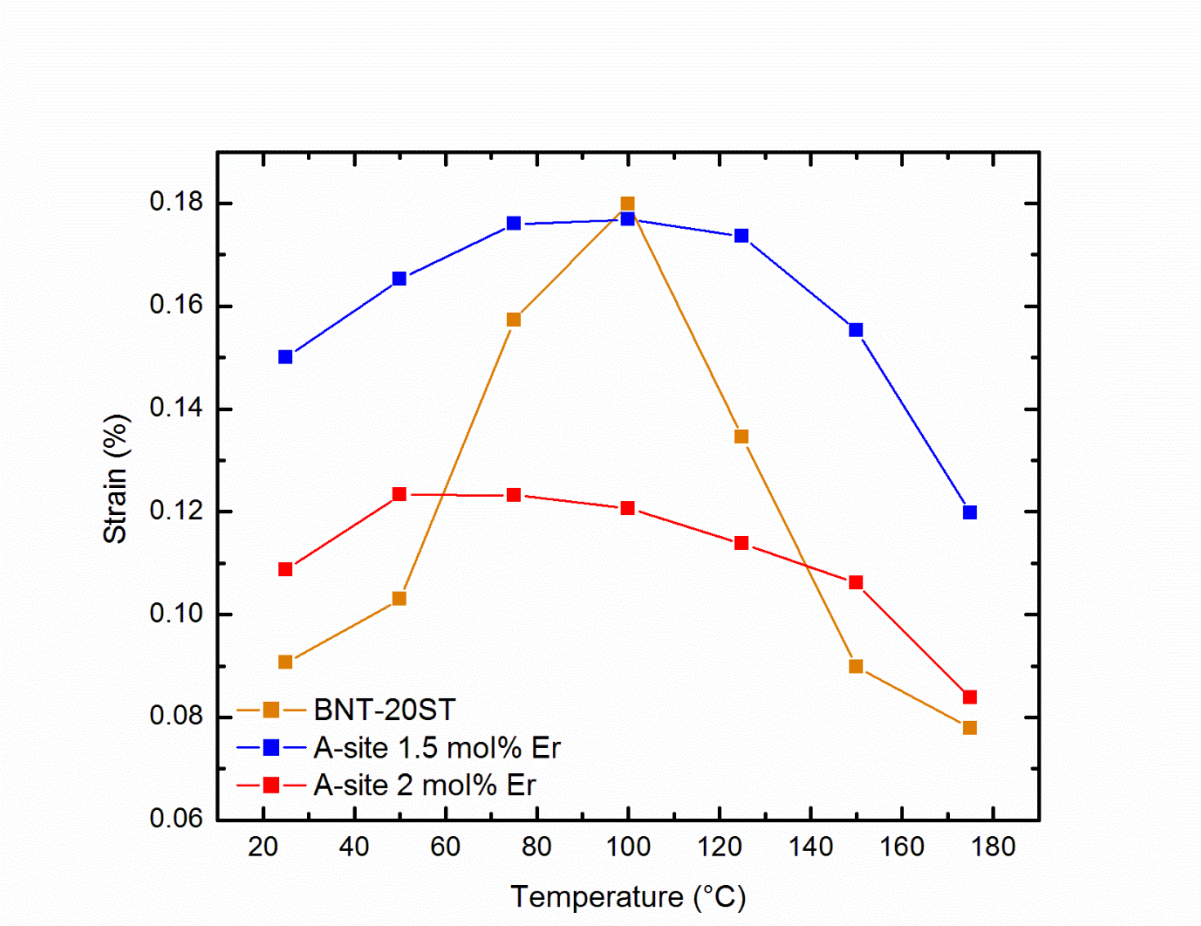
Strain (%)
0.18
0.16
0.14
0.12
0.10
0.08
0.06
20
40
60
80
100
120
140
160
180
Temperature (°C)
BNT-20ST
A-site 1.5 mol% Er
A-site 2 mol% Er

Figure 8